



Contents lists available at ScienceDirect

International Journal of Impact Engineering

journal homepage: www.elsevier.com/locate/ijimpeng

Concepts for enhanced energy absorption using hollow micro-lattices

A.G. Evans^a, M.Y. He^{a,*}, V.S. Deshpande^b, J.W. Hutchinson^c, A.J. Jacobsen^d, W.B. Carter^d^a Materials Department, College of Engineering, UCSB, CA 93106, USA^b Engineering Department, Cambridge University, Trumpington St, Cambridge CB2 1PZ, UK^c School of Engineering and Applied Sciences, Harvard University, Cambridge, MA 02138, USA^d HRL Laboratories, Malibu, CA 90265, USA

ARTICLE INFO

Article history:

Received 24 July 2009

Received in revised form

17 February 2010

Accepted 30 March 2010

Available online 11 April 2010

Keywords:

Energy absorption

Impulse

Cellular medium

Micro-lattices

Finite element

ABSTRACT

We present a basic analysis that establishes the metrics affecting the energy absorbed by multilayer cellular media during irreversible compaction on either a mass or volume basis. The behaviors at low and high impulse levels are distinguished through the energy dissipated in the shock. The overall mass of an energy absorbing system (comprising a cellular medium and a buffer) is minimized by maximizing the non-dimensional dissipation per unit mass parameter for the cellular medium, $\Lambda \equiv U_m \rho_s / \sigma_Y$, where U_m is the dissipation per unit mass of the cellular medium, ascertained from the area under the quasi-static compressive stress/strain curve, σ_Y the yield strength of the constituent material and ρ_s the density of the material used in the medium. Plots of Λ against the non-dimensional stress transmitted through the medium, σ_{tr} / σ_Y demonstrate the relative energy absorbing characteristics of foams and prismatic media, such as honeycombs. Comparisons with these benchmark systems are used to demonstrate the superior performance of micro-lattices, especially those with hollow truss members. Numerical calculations demonstrate the relative densities and geometric configurations wherein the lattices offer benefit. Experimental results obtained for a Ni micro-lattice with hollow members not only affirm the benefits, but also demonstrate energy absorption levels substantially exceeding those predicted by analysis. This assessment highlights the new opportunities that tailored micro-lattices provide for unprecedented levels of energy absorption for protection from impulsive loads.

© 2010 Elsevier Ltd. All rights reserved.

1. Introduction

Concepts for protecting structures from impulsive loads are of current interest. The prototypical threat comprises a shock in air characterized by an overpressure p_0 with associated impulse/area, I . For protection against the overpressure, an intervening medium is required that reduces the pressure from p_0 to a level below a damage threshold, σ_{th} . To achieve this, the medium must be capable of *large volume decrease at constant pressure* (Fig. 1) [1,2] (thereupon extending the impulse duration). Dense solids and fluids are not suitable because they are nearly incompressible. Appropriate materials include low-density cellular solids such as reticulated polymers [3], metal foams [1], pre-crushed honeycombs [3] and lattice solids [4], all with relative density, $\bar{\rho}$, in the 0.1–10% range and densification strains preferably exceeding 80%. Rectification is required by means of a planar buffer, mass/area m_b , positioned to face the shock (with the compressible medium

attached) [1,2]. The buffer acquires a momentum per area, M , equal to the transmitted impulse per unit area, I_{trans} , with associated kinetic energy/area, $KE = M^2/2 m_b$ [1]. This kinetic energy must either be dissipated by plastic deformation or stored elastically in the medium. The research objective in this area is to seek a medium that dissipates this KE at lowest possible mass/area, while not transmitting a stress greater than σ_{th} – a design constraint dictated by the nature of the structure being protected. We examine the potential of all known classes of cellular materials for attaining this objective and reveal a new regime wherein energy absorption per unit mass is maximized by using hollow micro-lattices, a consequence of their favorable topological characteristics.

While cellular materials such as stochastic foams and honeycomb are readily available, fabrication of appropriate micro-lattice structures has been challenging. As a consequence, experimental investigation of their energy absorption capability has been limited to solid truss geometries [5] or hollow-tube geometries [6] with discontinuous node connectivity. Recent developments have provided a new fabrication capability for realizing micro-lattices with unit cells in the 0.1 to > 10 mm range [7–9]. These structures have nearly ideal, truss-like geometries with linear truss

* Corresponding author. Tel.: +1 805 8936037; fax: +1 805 8938486.
E-mail address: ming@engineering.ucsb.edu (M.Y. He).

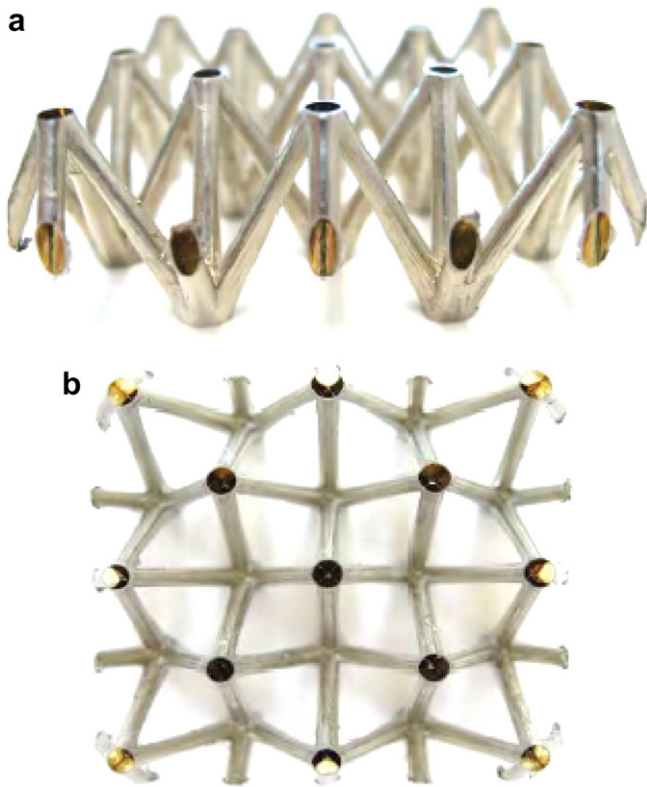


Fig. 2. (a) A side view, and (b) a top view image of a hollow Ni micro-lattice.

lattices. While the assessment is strictly applicable to multilayer cellular media that experience layer-by-layer sequential dynamic crushing, some of the energy absorption mechanisms are elucidated through simulations and measurements conducted on single layer micro-lattices.

2. Metrics

2.1. The minimum thickness of the cellular medium

The objective is to provide an analysis of the dynamic crushing of a cellular medium attached to a buffer. The medium is presumed to deform with “ideal” mechanical response (Figs. 1 and 3a), characterized by a constant unidirectional crushing stress, σ_{pl} , with strain at densification, ϵ_D . The major features governing the minimum thickness of the cellular medium, h_{min} , are presented in detail in the Appendix and with two non-dimensional parameters governing the response:

- Ratio of the mass of the cellular medium to that for the buffer, $\Pi \equiv h\rho_s\bar{\rho}\epsilon_D/m_b$, where h is the thickness of the crushable medium
- Ratio of the static to the dynamic strength of the cellular medium, $\Psi \equiv \sigma_{pl}m_b^2/M^2\rho_s\bar{\rho}$

where ρ_s is the density of the parent material and $\bar{\rho}$ the relative density of the cellular material. Based on the analysis, two regimes have been ascertained based on Π : *regime I* is essentially quasi-static while *regime II* is dynamic (Fig. 4).

2.1.1. Regime I

When $\Pi \leq 2$, shock effects in the medium are minimal, and the maximum dissipation/area is quasi-static, with $U = \sigma_{pl}\epsilon_D h$.

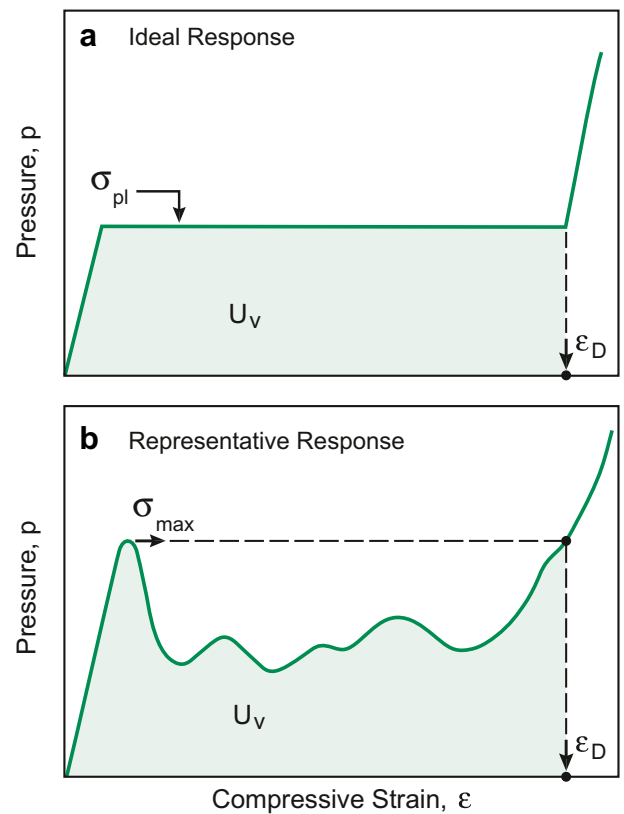


Fig. 3. Response of cellular solids to compression. (Top) “Ideal” behavior found in some foams. (Bottom) Actual behavior found in lattice solids and prismatic systems.

Equating the dissipation to the kinetic energy gives the minimum thickness to arrest the buffer as:

$$h_{min} = \frac{M^2}{2m_b\sigma_{pl}\epsilon_D} \quad (1a)$$

or, in terms of the foregoing non-dimensional parameters,

$$\Pi_{min} = 1/2\Psi \quad (1b)$$

where $\Pi_{min} \equiv h_{min}\rho_s\bar{\rho}\epsilon_D/m_b$.

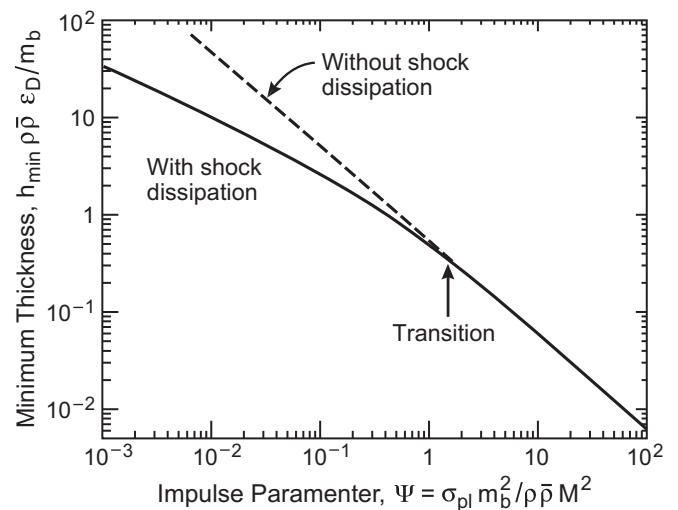


Fig. 4. The minimum thickness of a cellular medium needed to absorb the KE from an impulse.

Provided that the actual thickness, h , exceeds h_{\min} , the pressure imparted to the structure does not exceed σ_{pl} . Accordingly, by choosing $\sigma_{\text{pl}} < \sigma_{\text{th}}$ the structure is protected. When $h < h_{\min}$, the medium densifies before the buffer arrests and much larger pressures are transmitted when the buffer “slaps” into the structure. In regime I, the minimum thickness *decreases* as the buffer mass/area increases (1a) leading to a minimum in the total mass, elaborated below.

2.1.2. Regime II

When $\Pi \geq 2$, a shock develops in the medium. Because of the density and stress discontinuity across the shock, additional energy is absorbed [10,11]. The minimum thickness (Fig. 4) is smaller than that estimated by extrapolating from regime I and given by

$$\Pi_{\min} \approx 1/\sqrt{\Psi} \quad (2a)$$

or, in dimensional terms:

$$h_{\min} \approx \frac{M}{\sqrt{\rho_s \bar{\rho} \sigma_{\text{pl}} \epsilon_D}} \quad (2b)$$

Now, the minimum thickness of the cellular medium is *independent* of the mass per unit area of the buffer as elaborated below and in the Appendix.

2.2. The minimum mass for the system

The system mass is dependent on the impulse in accordance with the foregoing two regimes. In *regime I*, a minimum exists in the total (buffer and cellular medium) mass per area to mitigate the overpressure (Appendix) given by:

$$m_{\text{total}}^{\min} = M \sqrt{\frac{2\bar{\rho}\rho_s}{\sigma_{\text{pl}}\epsilon_D}} \equiv M \sqrt{\frac{2}{U_m}} \quad (3)$$

where $U_m \equiv \sigma_{\text{pl}}\epsilon_D/\rho_s\bar{\rho}$ is the *quasi-static* energy absorbed *per unit mass* of the cellular medium. At higher impulse levels, in *regime II*, the total mass is (Appendix)

$$m_{\text{total}} = m_b + M\sqrt{1/U_m} \quad (4)$$

While there is no minimum, if the buffer mass is selected to satisfy the inequality

$$m_b \leq (\sqrt{2} - 1)M\sqrt{1/U_m} \quad (5)$$

the lowest weight system resides in *regime II*. Accordingly, *maximizing* U_m always *minimizes* the overall weight. This is achieved by selecting constituents with lowest possible density, configured within architectures that experience “ideal” plateau response up to large densification strains.

2.3. Non-ideal crushing

Among the available cellular media, many compress with an initial peak, associated with member buckling, followed by an oscillating stress/strain response as the medium compresses (Fig. 3b) [3]. This response is undesirable because the stress transmitted through the medium is σ_{peak} , while the dissipation occurs at a lower stress. Consequently, the objective is to seek media with lowest possible density, $\rho_s\bar{\rho}$, that compress to a large densification strain, ϵ_D without a significant initial peak.

2.4. Media with yield governed crushing

When *members yield before buckling*, the non-dimensional dissipation/mass parameter that distinguishes the topology from the material properties is:

$$\Lambda = \frac{U_m \rho_s}{\sigma_Y} \equiv \frac{\sigma_{\text{pl}}}{\sigma_Y} \frac{\epsilon_D}{\bar{\rho}} \quad (6)$$

with σ_Y the yield strength of the constituent material. The preferred topology is that providing the requisite $\sigma_{\text{pl}}/\sigma_Y$ at the *lowest relative density*. Expressing the crushing strength through a generalized power law [3];

$$\sigma_{\text{pl}}/\sigma_Y = \zeta \bar{\rho}^n \quad (7a)$$

(with n between 1 and 2), the dissipation becomes

$$\Lambda = \zeta \epsilon_D \bar{\rho}^{n-1} \quad (7b)$$

Thus, *the smaller the exponent, n , the greater the energy absorbed/mass*. This straightforward principle rationalizes the trends in energy absorption among different topologies. Note that, for lattice topologies with $n = 1$, Λ is essentially *independent of the relative density*.

By equating the loads required for elastic buckling and yielding, it has been demonstrated that truss-based cellular media are yield (rather than buckling) dominated at relative densities that approximately satisfy [3],

$$\bar{\rho} > 36\epsilon_Y^2 \quad (8)$$

where ϵ_Y is the yield strain for the constituent material. For metals (with $\epsilon_Y \approx 10^{-3}$) yielding invariably predominates. Moreover, even for polymers ($\epsilon_Y \approx 10^{-2} \rightarrow 10^{-1}$), only systems with exceptionally low $\bar{\rho}$ are buckling limited.

3. Benchmarks

Stochastic media such as foams are relatively isotropic. Those whose cell walls yield by plastic bending before elastically buckling have a plateau stress that scales as [3]:

$$\sigma_{\text{pl}}/\sigma_Y \approx 0.3\bar{\rho}^{3/2} \quad (9a)$$

giving non-dimensional dissipation/mass:

$$\Lambda \approx 0.3\bar{\rho}^{1/2}(1 - 1.4\bar{\rho}). \quad (9b)$$

where we have taken $\epsilon_D = 1 - 1.4\bar{\rho}$.

A cross plot of Λ against the non-dimensional transmitted stress, $\sigma_{\text{pl}}/\sigma_Y$, characterizes *all foams at all viable relative densities* (Fig. 5). Each $\bar{\rho}$ is represented by a single point on the curve, as indicated on the figure.

Prismatic systems are anisotropic. Honeycombs are illustrative. In the transverse orientation, the plateau stress is [3]:

$$\sigma_{\text{pl}}/\sigma_Y \approx 0.5\bar{\rho}^2 \quad (10a)$$

such that (Fig. 5)

$$\Lambda \approx 0.5\bar{\rho}(1 - 1.4\bar{\rho}) \quad (10b)$$

Relative to foams, because of the larger exponent n , the energy absorbed at specified transmitted stress is *lower*.

In the axial direction, the peak stress is [3,12]:

$$\sigma_{\text{peak}}/\sigma_Y \approx 5.2\bar{\rho}^{5/3} \quad (11)$$

This peak is followed by oscillations at lower average stress, $\lambda\sigma_{\text{peak}}$, such that the energy absorption has the form:

$$\Lambda \approx 5.2\lambda\bar{\rho}^{2/3}(1 - 1.4\bar{\rho}) \quad (11d)$$

Results for $\lambda = 1/3$ are plotted on Fig. 5. The extreme anisotropy limits the use of prismatic structures when off-axis loadings are likely.

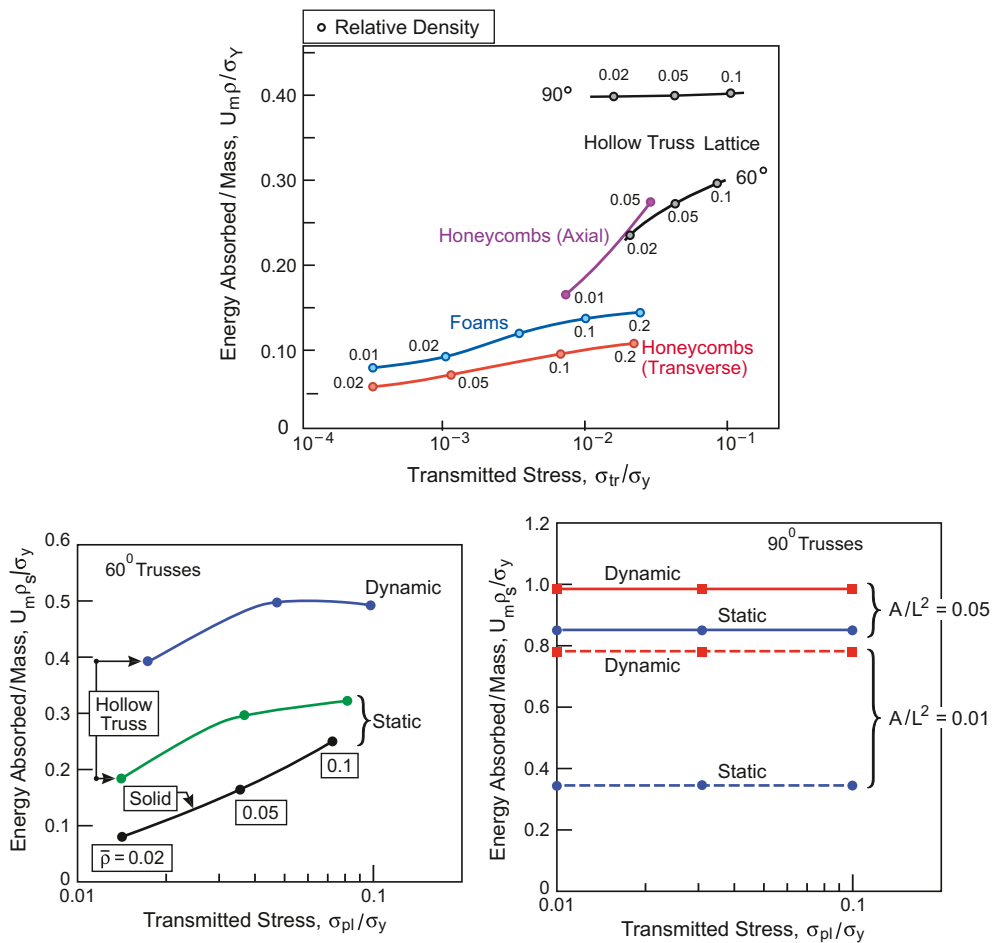


Fig. 5. Relationships between the energy absorbed/mass as a function of the stress transmitted through the medium: presented in a non-dimensional form that distinguishes the effects of topology from the influence of material properties. (Top) Comparison between hollow truss micro lattices and conventional cellular media. (Bottom). Results for a range of solid and hollow truss lattices: both quasi-static and dynamic. For all the hollow truss, $R/t = 5$.

4. Analysis of micro-lattices

4.1. Configurations and geometric variables

The HRL micro-lattice consists of an ensemble of pyramidal truss members of radius R , wall thickness t , length L with an included angle, $\theta = 60^\circ$ (see Fig. 2), attached at the nodes. Because the response to compression is characterized by the post-buckling deformation, the following geometric parameters are important: (i) The aspect ratio A/L^2 (with L the member length and A the cross-sectional area). (ii) The relative wall thickness, R/t . (iii) The orientation of the truss relative to the crush axis, θ . For a system with $\theta = 60^\circ$, the relative density is given by

$$\bar{\rho} = \frac{16}{\sqrt{3}} \frac{A}{L^2} \quad (12)$$

where

$$A \approx 2\pi Rt$$

4.2. Methods and preliminary assessments

For tractability the analysis is restricted to a single layer lattice, with the understanding that the results can be used to predict the behavior of a multilayer by using a shock propagation analysis (Appendix). Several unit cell configurations and numerical techniques have been explored (Fig. 6). Beam elements (Fig. 6a) are

unable to capture local plastic buckling (wrinkling). Consequently, unit cells with 3D shell elements (exemplified by the pyramidal truss Fig. 6b) have been used, as well as a single member of the pyramid (Fig. 6c) with symmetry boundary conditions. The commercial finite element code, ABAQUS/Explicit is used for the finite element simulations. A convergence study shows a mesh of 5000 3D shell elements (S4R, 64 (hoop) \times 80 (axial)) for a single tube gives accurate results.

The calculations are conducted for a material with properties resembling Al 7076 T6: albeit that the normalizations render universality. The material is assigned bilinear stress versus strain response, with moderate strain hardening (tangent modulus, $E_t/E = 0.01$), yield strain, $\epsilon_Y = 6 \times 10^{-3}$ and Young's modulus, $E = 70$ GPa. In all calculations the truss members are loaded in axial compression with fixed ends. The calculations are continued to large strains to capture densification.

4.3. Eigenmodes

Before proceeding, an eigenvalue analysis has been used to delineate the buckling modes. The analysis is elastic. Its purpose is to reveal the various competing shapes of the plastic buckling modes and not provide an estimate of the load carrying capacity. Moreover, imperfections in the shape of these eigenmodes are introduced in the analysis to ensure that realistic load-deflection behavior is triggered. Three classifications emerge: (i) global buckling, (ii) axi-symmetric and (iii) non-axisymmetric local

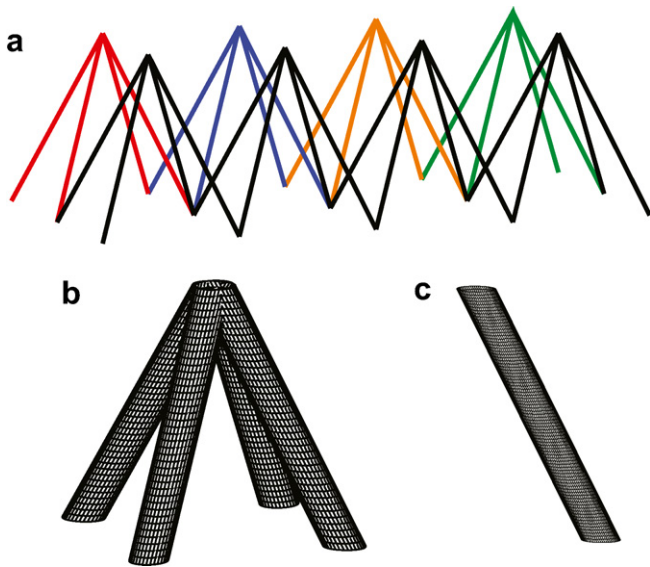


Fig. 6. Finite element schemes: (a) beam elements for 4 by 2 cells, (b) 3D shell elements, pyramidal truss unit cell, (c) 3D shell elements, single member 1/4 cell.

buckling (wrinkling). These modes for the plastic buckling of tubes have previously been classified in accordance with the mechanism map depicted on Fig. 7 [16].

4.3.1. Slender trusses

characterized by $A/L^2 = 0.01$, $R/t = 3$ (for $\theta = 90^\circ$) and by $\bar{\rho} = 2\%$, $A/L^2 = 0.0015$, $R/t = 5$ (for $\theta = 60^\circ$). The lowest two eigenmodes involve global buckling (Figs. 8a and 9a): followed by axisymmetric local buckling (Tables 1 and 2).

4.3.2. Stubby trusses

Characterized by $A/L^2 = 0.05$, $R/t = 5$ (for $\theta = 90^\circ$), and $\bar{\rho} = 5\%$ and $\bar{\rho} = 10\%$, $A/L^2 = 0.0075$, $R/t = 5$ (for $\theta = 60^\circ$). The lowest two eigenmodes correspond to non-axisymmetric local buckling, followed closely by axisymmetric modes (Figs. 8b and 9b). The lowest mode ascertained for the pyramidal cell (Fig. 9) is consistent with that found upon testing a polymer micro-lattice (Fig. 10). A

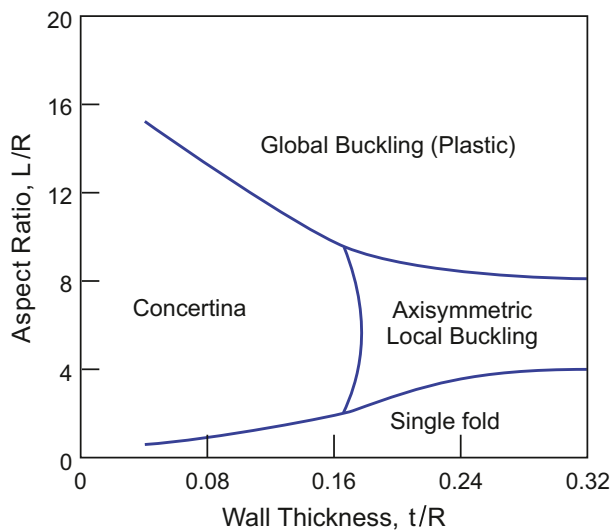


Fig. 7. Failure mechanism map for hollow 90° lattice members tested in compression [16].

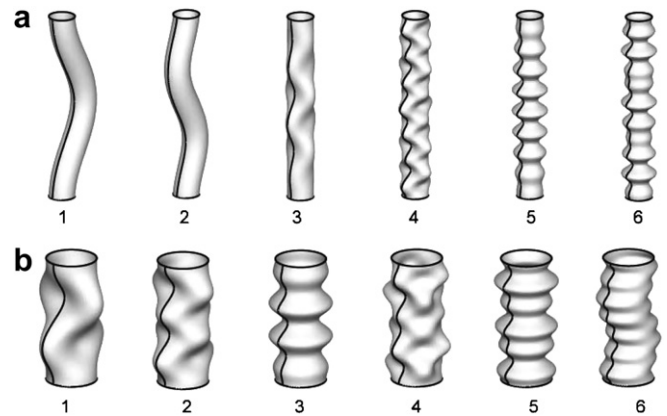


Fig. 8. The six Eigenmodes with lowest buckling stress for the 90° hollow tube. The stresses are given in Table 1. (Top) Slender members, $A/L^2 = 1\%$, $R/t = 3$: The two lowest modes refer to global buckling. The other four are for local buckling in axisymmetric and non-axisymmetric modes. (Bottom) Stubby members $A/L^2 = 5\%$, $R/t = 5$: all modes involve local buckling.

comparison among the eigenmodes for the pyramidal truss unit cell and the single member (Fig. 11) affirms that the buckling stresses and the modes are essentially the same.

4.4. Imperfections

To obtain viable predictions of plastic buckling, imperfections must be incorporated. The procedure adopted is based on that previously used for predicting the buckling of sandwich panel cores [17]. The first thirty eigenmodes are ascertained and initial imperfections are introduced to ensure that both global and local buckling effects are captured. For most of the calculations presented below, the imperfections have amplitude 1/10th the shell thickness, $\xi \equiv w_{max}/t = 0.1$, where w_{max} is the maximum imperfection amplitude.

4.5. Basis for assessment

Extensive work on the energy absorption capabilities of cylindrical metal tubes in the post-buckling range has been reported [18] with application to automotive crashworthiness. The relevance of this prior work to the lattice cores is limited because, in the HRL

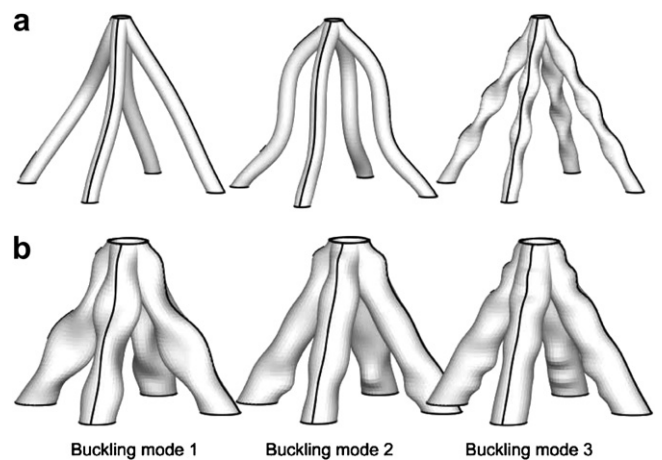


Fig. 9. Three lowest Eigenmodes for the pyramidal truss unit cell with $R/t = 5$. The corresponding buckling stresses are summarized on Table 2. (Top) Low relative density, $\bar{\rho} = 2\%$. The lowest two coincide with global buckling, while the third involves non-axisymmetric local buckling. (Bottom) higher relative density, $\bar{\rho} = 10\%$: all three modes are local.

Table 1
Eigenvalues for $\theta = 90^\circ$ hollow trusses.

Eigen modes	$A/L^2 = 0.01, R/t = 3$	
	Mode	σ_{bk}/E
(a)		
1	Global buckling	0.071
2	Global buckling	0.109
3	Non-axisymmetric local buckling	0.133
4	Non-axisymmetric local buckling	0.163
5	Axisymmetric local buckling	0.172
6	Axisymmetric local buckling	0.177
(b)		
1	non-axisymmetric local buckling	0.092
2	Non-axisymmetric local buckling	0.104
3	Axisymmetric local buckling	0.113
4	Non-axisymmetric local buckling	0.130
5	Axisymmetric local buckling	0.135
6	Non-axisymmetric local buckling	0.160

lattice, most core members are not aligned perpendicular to the crush direction. Depending on stubbiness and R/t , core members display axial modes in the early stages of buckling (not unlike that experienced by a tube designed for energy absorption in normal crush) but this mode inevitably gives way to lateral buckling [16]. Design of the core members to sustain energy absorption capabilities during lateral buckling is central to the identification of effective micro-lattice structures.

4.6. Truss deformations: $\theta = 90^\circ$

The stress/strain curves have the general form depicted on Fig. 12, comprising four primary phenomena, consistent with prior assessments [16].

- (i) The members yield at stress,

$$\sigma/\bar{\rho}\sigma_Y = 1. \tag{13}$$

- (ii) Strain hardening ensues followed by the onset of plastic buckling. The peak in non-dimensional stress is slightly larger than unity: $\sigma_{peak}/\bar{\rho}\sigma_Y \approx 1.2$.
- (iii) Plastic buckling is followed by softening at rate $d\sigma/d\epsilon$ that depends sensitively on the slenderness.
- (iv) For stubbier members, contact occurs at intermediate strain levels, as the tube crushes, causing a rise in the stress.
- (v) Once the system begins to densify, an effective densification strain, ϵ_D , is reached (Fig. 3b).

Table 2
Eigenvalues for the pyramidal unit cell.

Eigen modes	$\bar{\rho} = 2\%$		$\bar{\rho} = 10\%$	
	Mode	$\sigma_{bk}/E\bar{\rho}$	Mode	$\sigma_{bk}/E\bar{\rho}$
(a) Eigenvalues for the pyramidal unit cell				
1	Global buckling	0.023	Non-axisymmetric local buckling	0.062
2	Global buckling	0.041	Non-axisymmetric local buckling	0.066
3	Non-axisymmetric local buckling	0.059	Non-axisymmetric local buckling	0.071
(b) Comparison of unit cell with single member, $\bar{\rho} = 5\%$				
	Unit Cell		Single member	
1	Global buckling	0.049	Global buckling	0.049
2	Non-axisymmetric local buckling	0.060	Non-axisymmetric local buckling	0.059
3	Non-axisymmetric local buckling	0.063	Non-axisymmetric local buckling	0.064

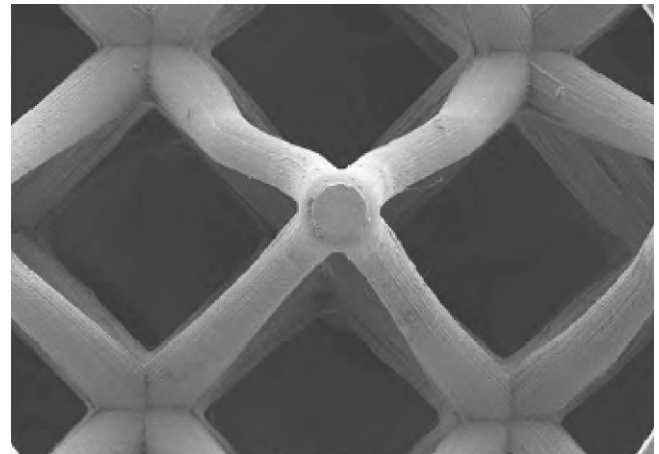


Fig. 10. The buckling mode for a polymer micro-lattice, showing the correspondence with the first mode depicted on Figs. 9 and 11.

Calculations have been conducted for slenderness in the range, $0.0015 \leq A/L^2 \leq 0.01$, wall thickness, $3 \leq R/t \leq 10$, and imperfection amplitudes $0 \leq \xi \leq 0.2$. A basic set of results is presented on Figs. 13 and 14. The effects of the wall thickness, R/t , and of the imperfection amplitude are quite small over the range assessed. Conversely, *slenderness substantially affects the response*. The differing effects are evident in the deformations, in conjunction with the associated stress/strain curves. When the members are relatively *stubby* (Fig. 13), a short wavelength shell mode is induced. The ensuing wrinkles have a characteristic wavelength smaller than the tube diameter, so that several occur over the length. Absent imperfections, axi-symmetric modes prevail (Fig. 13a and b), but become non-axi-symmetric when imperfections are introduced (Fig. 13c and d). These buckles develop by circumferential plastic stretching, dissipating substantial energy, and resulting in low softening rates. The softening is somewhat imperfection dependent because the non-axi-symmetric modes reduce the requirement for plastic stretching, increasing the softening rate. The more *slender tubes* experience global buckling over the range of wall thickness and imperfections examined (Fig. 14). The associated large-scale bending leads to rapid softening. The stresses rise again only when contact begins, at strains of order 70%.

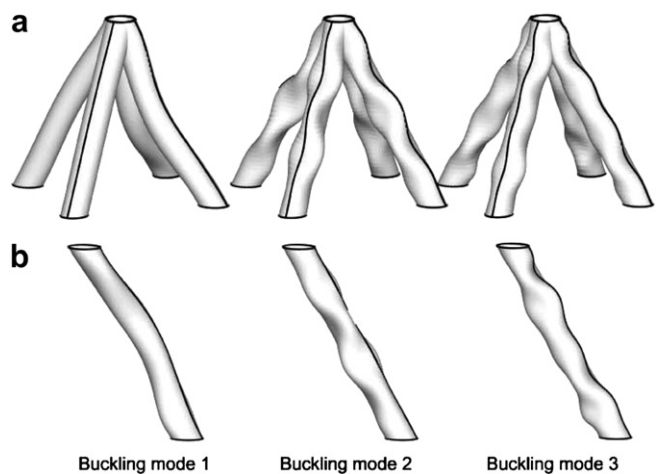


Fig. 11. The close correspondence between the Eigenmodes for the pyramidal truss unit cell (top) and a single member subject to symmetry boundary conditions (bottom): relative density $\bar{\rho} = 5\%$, $R/t = 5$.

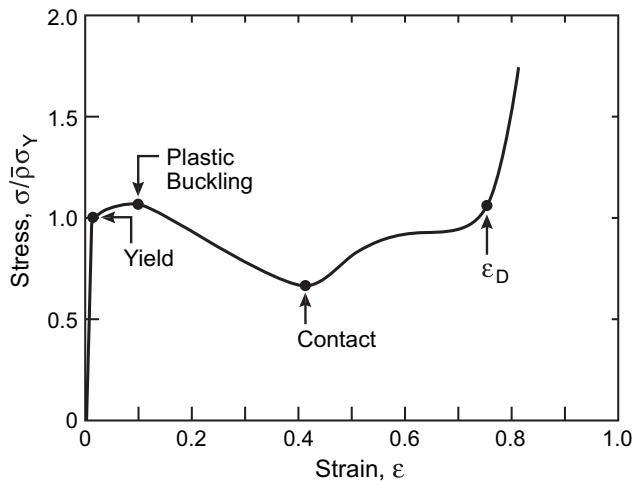


Fig. 12. A representative stress/strain curve found for hollow truss micro-lattices with 90° truss orientation.

The forgoing stress/strain curves have been converted into estimates of the energy absorbed per unit mass, by ascertaining the areas under the curves, in the manner depicted on Fig. 3. The results are superimposed on Fig. 5. The energies are essentially invariant with the transmitted stress, for the reason anticipated by (7b): namely, for these lattices, the peak stress scales linearly with the relative density. Note that, in the absence of softening after plastic buckling, (7b) and (13) give the upper bound:

$$A \approx \epsilon_D \approx 0.8 \quad (14)$$

4.7. Truss deformations: $\theta = 60^\circ$

The general stress/strain response is similar to that for the slender members at $\theta = 90^\circ$. The principal difference is that the initial peak occurs at a lower axial stress, $\sigma_{peak}/\bar{\rho}\sigma_Y \approx 0.75$, with minimal strain hardening (Fig. 15). The subsequent softening is quite extensive, and a strong function of the relative density (Fig. 15), as well as the wall thickness. The deformation patterns at low relative density ($\bar{\rho} = 2\%$), for imperfection amplitude (ratio of amplitude to shell thickness), $\xi = 0.1$, reveal the factors that govern the response (Fig. 16). Initially, the columns yield uniformly. Then, at strains of $\sim 5\%$, just beyond the stress peak, the members buckle in accordance with eigenmode 1 (Fig. 9). Upon further straining, lateral buckling occurs and kinks form at the region of highest curvature, resulting in rapid softening. In some cases, at strains of order 50–60%, the kinked regions make contact causing a small elevation in the stress. The softening rate diminishes appreciably as the relative density of the tubes increases (Fig. 15), because the mode changes from global buckling at low $\bar{\rho}$ to local buckling at higher $\bar{\rho}$ (Fig. 9). The energy absorbed per mass is plotted on Fig. 5 as a function of the relative density. Now, unlike the 90° response, the energy absorbed becomes $\bar{\rho}$ dependent, because of the associated change in buckling mode.

4.8. Rate effects

To assess the influence of inertial stabilization [17], the foregoing calculations have been repeated for compaction velocities of 100 m/s. Results obtained for slender 90° members highlight the primary effect (Fig. 17). Namely, global buckling is suppressed and replaced by wrinkling. The consequent energy absorption is thereby increased, as plotted on Fig. 5. There is a caveat regarding

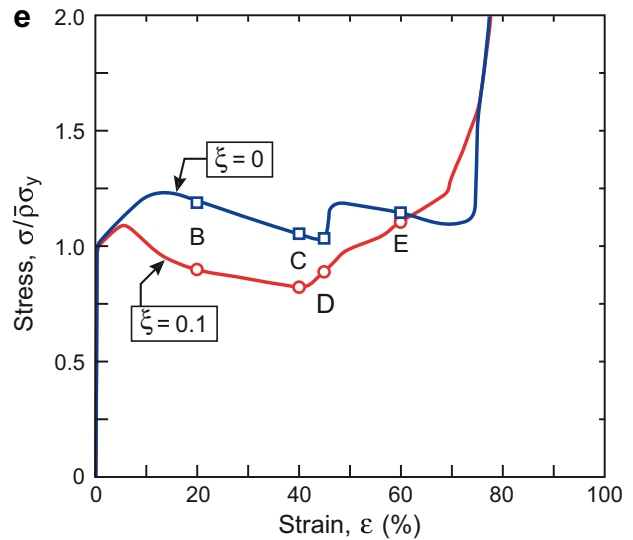
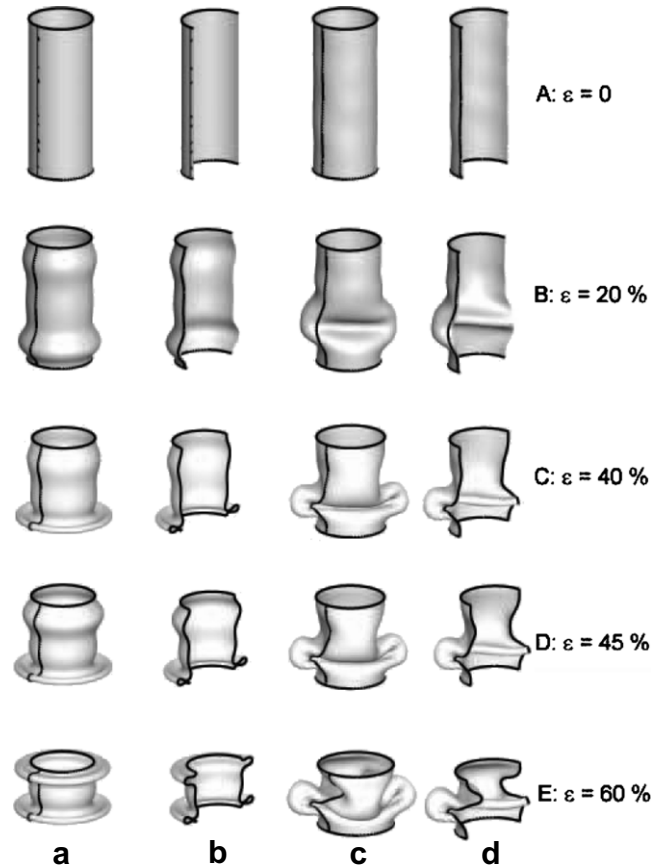


Fig. 13. Stress/strain response and deformation characteristics for a stubby 90° hollow tube, comparing a case without imperfections, $\xi = 0$ (upper left columns, a, b) to a case incorporating imperfections (upper right columns, c, d) with amplitude, $\xi = 0.1$ (described in the text): $R/t = 5$, $A/L^2 = 5\%$. The letters on the lower plots refer to the deformation responses shown on the upper figure. Note the circumferential plastic stretch at the location of the local buckles. Columns (a and c) show the deformations of the full tube. Columns (b and d) show mid-plane sections through the tube that reveal additional detail.

the overall energy absorption in a multilayer lattice. That is, the energy elevation is a part of the extra dissipation at the shock front (Fig. 4, Appendix) and should not be viewed as an additional contribution. Further evaluation of these dynamic phenomena will be addressed in continuing assessments.

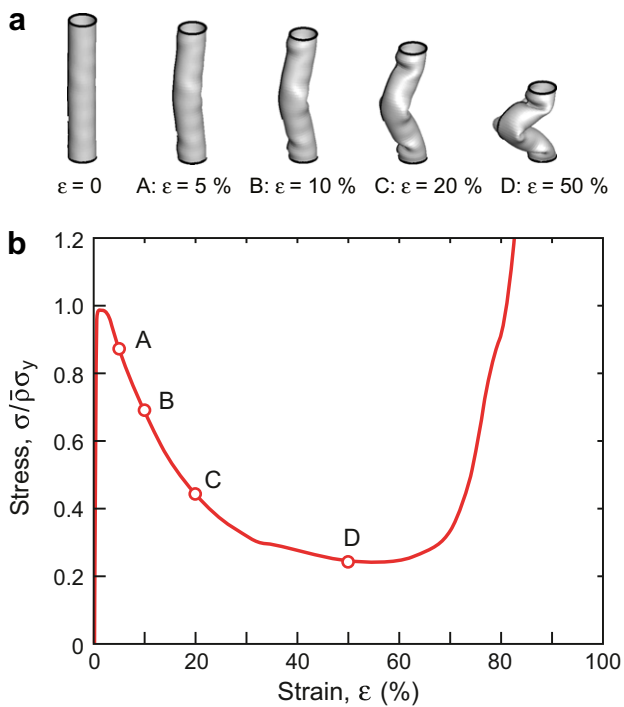


Fig. 14. Stress/strain response and deformation characteristics for a slender 90° hollow tube for a case incorporating imperfections with amplitude, $\xi = 0.1$ (described in the text): $R/t = 5$, $A/L^2 = 1\%$.

5. Experimental methods and measurements

5.1. Polymer micro-lattice template fabrication

Basic polymer micro-lattices were fabricated from an interconnected pattern of self-propagating photopolymer waveguides [7–9]. A mask with a square pattern of circular apertures was placed over the photo-monomer and exposed to four collimated beams, generated from a mercury arc lamp. Each collimated beam

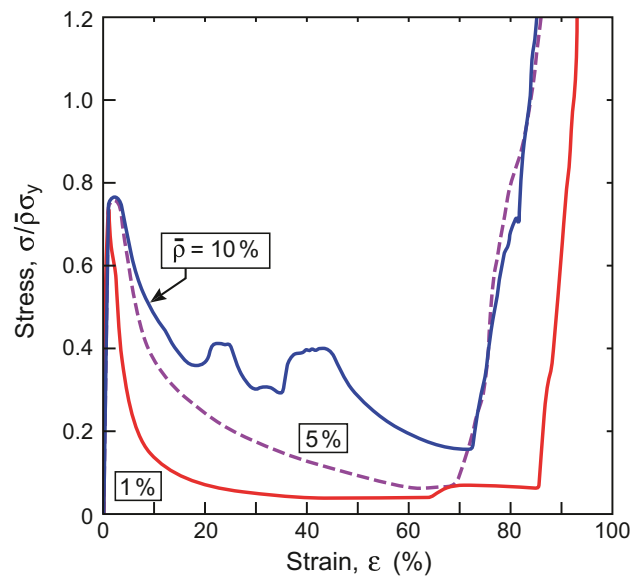


Fig. 15. Effects of relative density on the stress/strain response of a 60° pyramidal hollow truss lattice: $R/t = 10$.

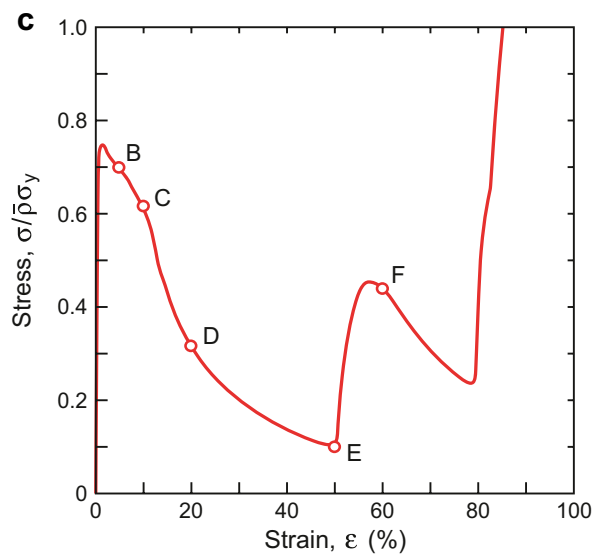
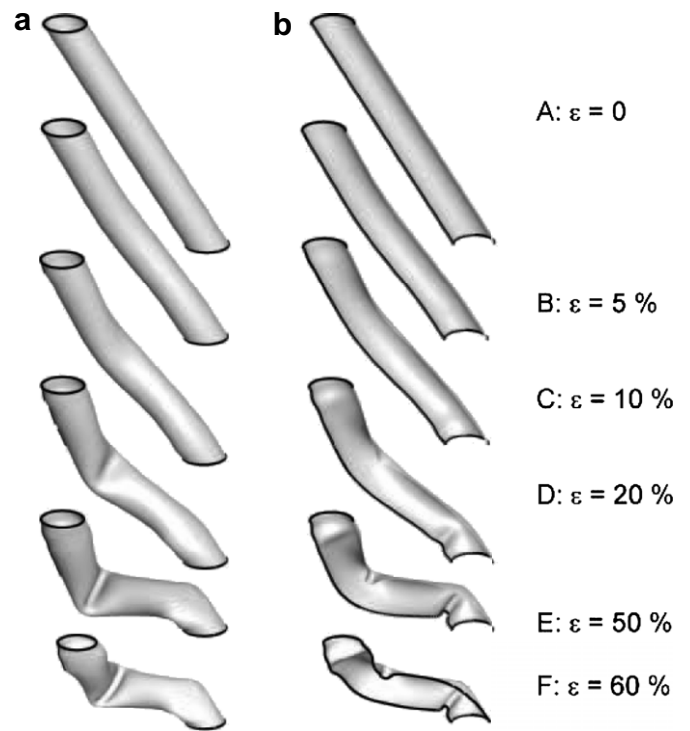


Fig. 16. Stress/strain response and deformation characteristics for a slender 60° hollow micro-lattice for a case incorporating imperfections with amplitude, $\xi = 0.1$: $R/t = 5$, $\bar{\rho} = 5\%$. The upper left figures (a) show the deformations of the full tube. The upper right figures (b) show mid-plane sections through the tube that reveal additional detail.

had a 40° incident angle, rotated 90° about the normal. A pyramidal unit cell was formed by choosing a depth of photomonomer coincident with the first nodal point.

5.2. Hollow Ni micro-lattice fabrication

The polymer micro-lattices were used as direct templates for electro-deposition of Ni. Initially, a conductive seed layer ($\sim 200 \text{ \AA}$ Ti followed by $\sim 2000 \text{ \AA}$ Au) was deposited by using an evaporator. The Ni was then electrodeposited within a commercial electro-forming solution. A platinum/rhodium wire, threaded on the outer

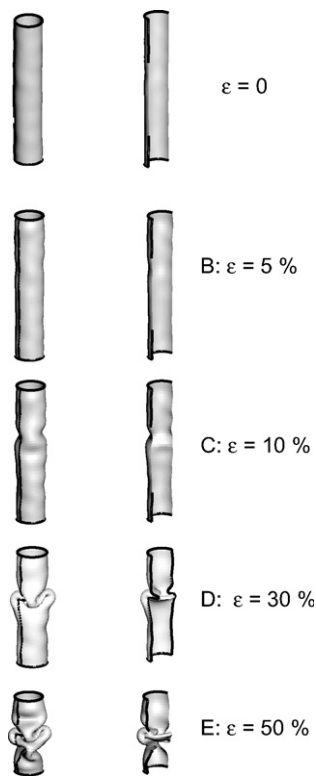


Fig. 17. Response of a slender 90° hollow truss to compression at 100 m/s. Note the absence of global buckling because of the inertial stabilization. The left figures show the deformations of the full tube. The right figures show mid-plane sections through the tube that reveal additional detail.

edge, formed the electrode connection. The plating was performed at 50 °C and $\sim 8.5 \text{ mA/cm}^2$. To achieve different coating thicknesses, two different samples were plated for 6 and 12 h, respectively. After electro-deposition, the top and bottom surfaces were removed to expose the underlying polymer at each node, as well as along the outer edges in contact with the electrode wire. The polymer was chemically etched in a base solution (3 M NaOH at 60 °C), creating the hollow tube Ni micro-lattice samples used for the mechanical measurements.

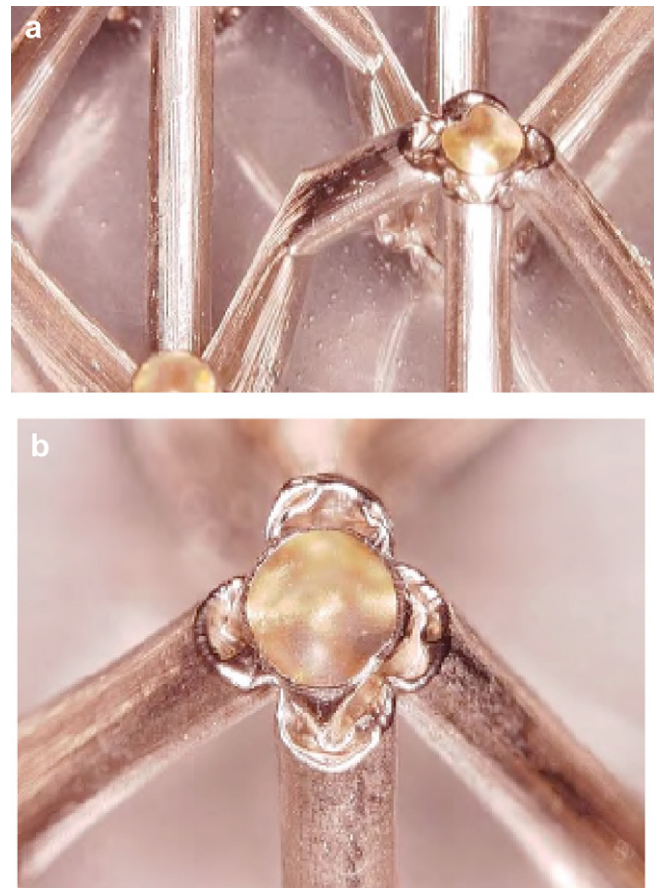


Fig. 19. The deformation modes in the Ni hollow truss micro-lattice at 20% compression. (a) Some members exhibit lateral buckling in the manner predicted by the simulations (Fig. 16). (b) Other members exhibit a concertina-wrinkling mode at the nodes but otherwise remain straight. This mode is attributed to a larger R/t near the nodes and is suspected as the source of the substantial extra energy dissipation.

5.3. Base properties of electroformed Ni

The Ni used for fabricating the lattices had a density of 8.9 g/cc. Nano-hardness tests conducted on the walls gave a Young's modulus, $E = 200 \text{ GPa}$. Micro-hardness measurements gave an inferred yield strength, $\sigma_Y \approx 300 \text{ MPa}$.

5.4. Compression measurements

Based on their mass and dimensions, samples plated for 6 and 12 h had relative density, $\bar{\rho} = 0.007$ and $\bar{\rho} = 0.014$, respectively. The top and bottom surfaces were bonded to thick steel face-sheets using a fast-setting epoxy to constrain the nodes from lateral displacement. Quasi-static compression tests were conducted using an MTS hydraulic load frame at a strain rate of $7 \times 10^{-4} \text{ s}^{-1}$. The compressive stress–strain responses for the two hollow Ni micro-lattice samples are shown in Fig. 18, indicating behavior similar to that presented on Fig. 3b: comprising an initial stress peak, followed by stress oscillations prior to densification at $\epsilon_D \approx 0.8$. Based in the preceding estimate of the yield strength and of the relative densities, the stress peak occurs at, $\sigma_{\text{peak}}/\bar{\rho}\sigma_Y \approx 1.2$, slightly larger (by 20–30%) than that predicted by the simulations. More significantly, the softening rate beyond the peak is *much less severe* than in the simulations, at the equivalent relative density. The consequence is that the energy absorbed/mass, $A \approx 1$ (beyond

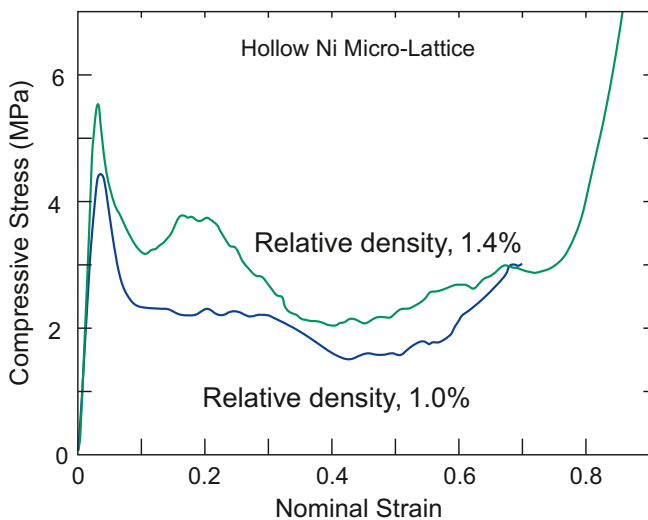


Fig. 18. Experimental measurements for a Ni hollow truss micro lattice (Fig. 2b).

the scale of Fig. 5), is about a factor 2 larger than that determined by simulation at the equivalent transmitted stress, $\sigma_{tr}/\sigma_Y \approx 10^{-2}$ ($\lambda \approx 0.4$). The implication is that the actual lattices have plastic dissipation mechanisms not elucidated in the simulations. To search for possibilities, partially compressed lattices have been imaged (Fig. 19). The images reveal that, while some members exhibit lateral buckling modes similar to predictions, a complementary local mode develops at some of the nodes. The associated local wrinkling is similar to the concertina mode identified in an earlier study [16] but remains to be understood. It is tentatively attributed to a larger R/t at the nodes. Given the implications for much greater energy absorption, this mode will be emphasized in future assessments.

6. Concluding remarks

Through a combination of simulations and experiments a metallic hollow wall micro-lattice has been identified that absorbs an unusually large energy per unit mass. The energy absorption is governed by the plastic deformations that occur subsequent to plastic buckling. In the simulations, conducted with walls of uniform thickness, the lattice members exhibit lateral buckling and kinking, with ensuing (relatively) rapid softening. Nevertheless, relative to other cellular media having isotropic response, such as foams, the hollow wall micro-lattices absorb more than twice the energy per unit mass. More dramatically, experimental measurements performed on such lattices exhibit yet larger energy absorption than the simulated lattices, by another factor of two (more than 4–5 times that for foams). Preliminary observations performed on the compressed lattices indicate a local wrinkling mode in the vicinity of the nodes where R/t is larger. The associated concertina mode is surmised to be the source of the extra energy absorption. This exciting new development is the subject of ongoing research.

Appendix. Analysis of shock effects and design metrics

We seek to determine the minimum thickness $h = h_{\min}$ of a multilayer cellular medium needed to dissipate the kinetic energy $(1/2)m_b v_0^2$ of the buffer. The medium has initial density ρ and the compressive stress/strain characteristic (under uniaxial straining) as sketched in Fig. A1a: with a constant plateau stress σ_{pl} and a nominal densification strain ϵ_D . A plastic shock enters the medium from the impact face and travels at a speed $c(t)$. The incident portion, downstream of the shock, attains a velocity $v(t)$ (Fig. A1b). The distal portion, upstream, is at rest. At any instant, the medium is non-deforming except for a jump in compressive strain (magnitude ϵ_D) across the shock. After time t , the shock has traveled distance s , as measured in the un-deformed configuration. We proceed to analyze the shock employing a Lagrangian framework wherein all velocities and accelerations are measured with respect to a stationary reference frame. For this one-dimensional situation (with zero plastic Poisson ratio), the Cauchy and nominal stresses are identical and the equation of motion is:

$$\frac{\partial \sigma}{\partial X} = -\rho \frac{\partial^2 u}{\partial t^2} \quad (\text{A. 1})$$

where X is the position of material point in the un-deformed configuration, u is displacement, and σ the stress. Integrating (A. 1) over the range $0 \leq X \leq s$ and noting that the medium (and buffer) are rigid, gives the acceleration \dot{v} downstream of the shock as:

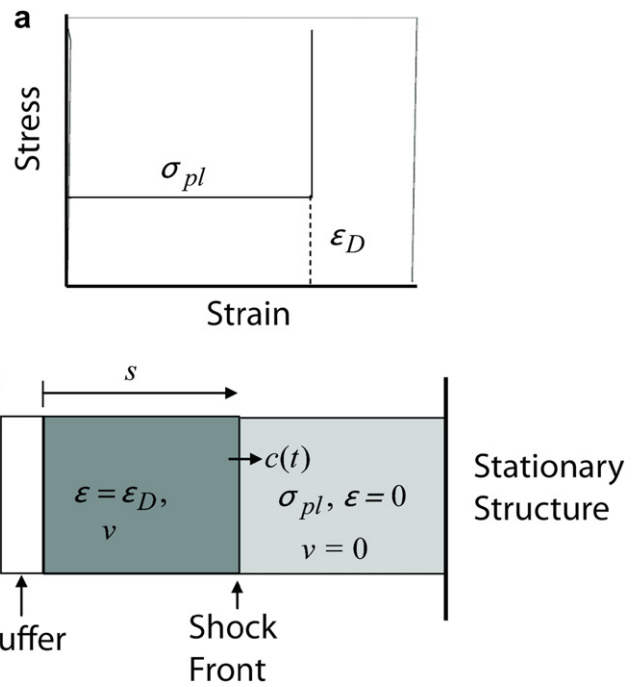


Fig. A1. (a) The stress/strain curve for the cellular medium. (b). The material state upstream and downstream from the shock front.

$$(m_b + \rho s)\dot{v} = -\sigma_d \quad (\text{A. 2})$$

Immediately upstream the stress is σ_{pl} . Momentum conservation across the shock dictates that [10]

$$\sigma_d - \sigma_{pl} = \rho c v \quad (\text{A. 3})$$

Furthermore, mass conservation implies that [10]

$$\dot{s} \equiv c = v/\epsilon_D \quad (\text{A. 4})$$

Combining (A. 2)–(A. 4) gives the overall governing ODE for the deformation as

$$\frac{m_b}{\rho} \ddot{s} + s\ddot{s} + \dot{s}^2 = \frac{\sigma_{pl}}{\rho \epsilon_D} \quad (\text{A. 5})$$

The initial conditions are $s = 0$ and $\dot{s} = v_0/\epsilon_D$ at time $t = 0$. When the deformation arrests, at time, $t = M/\sigma_{pl}$, then $s = s_{\text{final}}$ and we define $h_{\min} \equiv s_{\text{final}}$.

The non-dimensional groups are

$$\bar{s} \equiv \frac{s}{h}; \quad \bar{t} \equiv \frac{t v_0}{h}; \quad \dot{\bar{s}} \equiv \frac{\dot{s}}{v_0}; \quad \ddot{\bar{s}} \equiv \frac{\ddot{s} h}{v_0^2} \quad (\text{A. 6})$$

Substituting into (A. 5), the governing ODE becomes

$$\ddot{s}/\Pi + \bar{s} \ddot{\bar{s}} + \dot{\bar{s}}^2 = -\Psi/\epsilon_D^2 \quad (\text{A. 7a})$$

with initial conditions, $\bar{s} = 0$ and $\dot{\bar{s}} = 1/\epsilon_D$ at $\bar{t} = 0$. One of the associated non-dimensional parameters is the mass ratio for the cellular medium to the buffer

$$\Pi \equiv \frac{\rho h}{m_b} \quad (\text{A. 7b})$$

while the other is the ratio of the static to dynamic strength of the medium

$$\psi \equiv \frac{\sigma_{pl} m_b^2 \epsilon_D}{\rho M^2} = \frac{\sigma_{pl}}{\rho v_0^2 / \epsilon_D} \quad (\text{A. 7c})$$

The response is completely specified given the non-dimensional quantities, Π , ψ and ϵ_D . We iteratively solve (A. 7) for Π_{\min} such that $\bar{s} = 1$, when \bar{s} first attains zero. The numerical values are plotted on Fig. 4 as a function of ψ . Two regimes emerge.

Regime I ($\Pi \ll 1$)

wherein Eq. (A. 7) can be approximated as

$$\frac{\ddot{\bar{s}}}{\Pi} = -\frac{\psi}{\epsilon_D^2} \quad (\text{A. 8a})$$

This ODE can be solved analytically (with the foregoing initial conditions) to obtain

$$\dot{\bar{s}}^2 = \frac{1}{\epsilon_D^2} - \frac{2\psi\Pi}{\epsilon_D^2} \bar{s} \quad (\text{A. 8b})$$

Enforcing the condition that $\bar{s} = 1$ when $\dot{\bar{s}} = 0$, we obtain

$$\Pi_{\min} = 1/2\psi \quad (\text{A. 8c})$$

or, equivalently

$$h_{\min} = \frac{M^2}{2\sigma_{pl} m_b \epsilon_D} \quad (\text{A. 8d})$$

In this regime the buffer is much heavier than the cellular medium, whereupon inertial effects can be neglected and the quasi-static energy balance equation holds:

$$\sigma_{pl} \epsilon_D h_{\min} = (1/2) m_b v_0^2 \quad (\text{A. 9})$$

The minimum medium thickness decreases with increasing mass m_b of the buffer because the kinetic energy it acquires varies as, $M^2/2m_b$.

Regime II ($\Pi \gg 1$)

wherein Eq. (A. 7) can be approximated as

$$\bar{s} \ddot{\bar{s}} + \dot{\bar{s}}^2 = -\frac{\psi}{\epsilon_D^2} \quad (\text{A. 10})$$

with initial conditions $\bar{s} = 1/\Pi$ and $\dot{\bar{s}} = 1/\epsilon_D$ at $\bar{t} = 0$. These modified initial conditions ensure that, $\dot{\bar{s}} = -(II/\epsilon_D^2)(\psi + 1)$ at $\bar{t} = 0$, consistent with Eq. (A. 7). Again, Eq. (A. 10) can be solved analytically to give

$$\bar{s} = \frac{1}{\Pi} \sqrt{\frac{\psi + 1}{\psi + \epsilon_D^2 \dot{\bar{s}}^2}} \quad (\text{A. 11})$$

Substituting the condition that, when $\dot{\bar{s}} = 0$, $\bar{s} = 1$ we obtain

$$\Pi_{\min} = \sqrt{1 + \frac{1}{\psi}} \quad (\text{A. 12})$$

Recalling that this solution only holds for $\Pi \gg 1$, it is sufficient to approximate as

$$\Pi_{\min} \approx \frac{1}{\sqrt{\psi}} \quad (\text{A. 13a})$$

or equivalently

$$h_{\min} \approx \frac{M}{\sqrt{\rho \sigma_{pl} \epsilon_D}} \quad (\text{A. 13b})$$

In this regime the buffer has lower weight than the cellular medium, whereupon inertial effects are significant. The energy

absorbed significantly exceeds the quasi-static dissipation. This extra dissipation can be traced to the very high strain rates across the shock that give rise to, among other things: changes in the collapse mode of the individual cells, inertial stabilization of the struts, a change in the collapse mode from bending/buckling to axial stretching of the struts.

Equations (A. 3) and (A. 4) together specify that

$$\sigma_d = \sigma_{pl} + \rho \frac{v_0^2}{\epsilon_D} \quad (\text{A. 14})$$

Thus, the ratio Ω of the energy absorption under dynamic and quasi-static ($v_0 \rightarrow 0$) conditions is

$$\Omega = 1 + \frac{\rho v_0^2}{\sigma_{pl} \epsilon_D} \quad (\text{A. 15})$$

Namely, the energy absorption increases quadratic ally with increasing v_0 . A consequence is that, unlike *regime I*, h_{\min} is independent of m_b , because the increased energy absorption compensates for the increased kinetic energy of the buffer.

The asymptotic solutions, included in Fig. 4, affirm that Eqs. (A. 8c) and (A. 13a) are a good approximation for the full numerical solution in the ranges, $\Pi_{\min} \leq 2$ and $\Pi_{\min} > 2$.

Optimization of the protection system

It is of interest to minimize either the mass or volume of the entire protection system comprising the cellular medium and buffer. For this purpose, the buffer mass/thickness is treated as the free variable and we employ the analytical solutions for h_{\min} .

Minimum mass systems

The total mass/area of the protection system is

$$m_{\text{total}} = m_b + \rho h_{\min} \quad (\text{A. 16})$$

Regime I

Substituting for h_{\min} from Eq. (A. 8d) we obtain

$$m_{\text{total}} = m_b + \frac{\rho M^2}{2\sigma_{pl} m_b \epsilon_D} \quad (\text{A. 17})$$

Minimizing m_{total} with respect to m_b , gives the minimum mass of the total system as

$$m_{\text{total}}^{\min} = M \sqrt{\frac{2\rho}{\sigma_{pl} \epsilon_D}} \quad (\text{A. 18})$$

with $\Pi_{\min} = 1$ at the optimum. Recall that this regime applies when $\Pi_{\min} \leq 2$.

Regime II

Substituting for h_{\min} from Eq. (14) we obtain

$$m_{\text{total}} = m_b + M \sqrt{\frac{\rho}{\sigma_{pl} \epsilon_D}} \quad (\text{A. 19})$$

As h_{\min} is independent of m_b , there is no minimum for m_{total} . Recalling that Eq. (A. 13) is only valid for $\Pi_{\min} > 2$, gives the restriction that m_b satisfy

$$m_b < \frac{M}{2} \sqrt{\frac{\rho}{\sigma_{pl} \epsilon_D}} \quad (\text{A. 20})$$

To ensure that the minimum mass solutions are lighter than those for regime I we restrict solutions to the range

$$m_b \leq (\sqrt{2} - 1)M \sqrt{\frac{\rho}{\sigma_{pl}\epsilon_D}} \quad (\text{A. 21})$$

Whereupon, the overall minimum mass solution *always lies in regime II* and given by Eq. (A. 19) with m_b specified by Eq. (A. 21).

Minimum volume systems

In some applications it may be necessary to minimize the volume of the protection system. The volume/area (or equivalently, the thickness) is given by

$$V_{\text{total}} = \frac{m_b}{\rho_b} + h_{\text{min}} \quad (\text{A. 22})$$

where ρ_b is the density of the buffer material. We minimize V_{total} with respect to m_b .

Regime I

Substituting for h_{min} from Eq. (10b) we obtain

$$V_{\text{total}} = \frac{m_b}{\rho_b} + \frac{M^2}{2\sigma_{pl}m_b\epsilon_D} \quad (\text{A. 23})$$

Minimizing V_{total} with respect to m_b gives the minimum volume as

$$V_{\text{total}}^{\text{min}} = M \sqrt{\frac{2}{\rho_b\sigma_{pl}\epsilon_D}} \quad (\text{A. 24a})$$

with

$$\Pi_{\text{min}} = \rho/\rho_b \quad (\text{A. 24b})$$

Thus, the minimum volume solution is only valid for the choice, $\rho_b/\rho \geq 2$. This, constraint is practical, as we anticipate the density of most buffer plate materials to be more than twice that of the backing foam.

Regime II

In this regime the volume of the protection system is given by

$$V_{\text{total}} = \frac{m_b}{\rho_b} + M \sqrt{\frac{1}{\rho\sigma_{pl}\epsilon_D}} \quad (\text{A. 25})$$

Since h_{min} is independent of m_b , there is no minimum for V_{total} . The global minimum must ensure that the minimum V_{total} is less than or equal to the volume specified by Eq. (A. 24a), giving the additional constraint.

$$0 < m_b \leq M \left(\sqrt{2} - \sqrt{\frac{\rho_b}{\rho}} \right) \sqrt{\frac{\rho_b}{\sigma_{pl}\epsilon_D}} \quad (\text{A. 26})$$

Combining with Eqn (A. 20) gives the constraints on m_b as

$$m_b \leq \begin{cases} \frac{M}{2} \sqrt{\frac{\rho}{\sigma_{pl}\epsilon_D}} & \text{if } \frac{\rho_b}{\rho} \leq \frac{1}{2} \\ M \left(\sqrt{2} - \sqrt{\frac{\rho_b}{\rho}} \right) \sqrt{\frac{\rho_b}{\sigma_{pl}\epsilon_D}} & \text{if } \frac{1}{2} < \frac{\rho_b}{\rho} \leq 2 \\ \text{no solution} & \text{for } \frac{\rho_b}{\rho} > 2 \end{cases} \quad (\text{A. 27})$$

However, in most cases, it is impractical to obtain a material combination with $\rho_b \leq 2\rho$. Accordingly, we anticipate that practical designs will lie in regime I, given by Eq. (A. 24).

Choice of material

The mass of the protection system is minimized by choosing a cellular medium that maximizes its quasi-static energy absorption/mass, $U_m = (\sigma_{pl}\epsilon_D)/\rho$, with *no constraint* on the choice of the buffer material. The volume of the protection system is minimized by choosing a cellular medium that maximizes its quasi-static energy absorption/volume (σ_p/ϵ_D) *and* choosing a dense buffer material (high ρ_b).

References

- [1] Ashby MF, Evans AG, Fleck NA, Gibson LJ, Hutchinson JW, Wadley HNG. Metal foams, a design guide. Butterworth-Heinemann; 2000.
- [2] Wadley HNG, Dharmasena KP, He MY, McMeeking RM, Evans AG, et al. Prog Intl J Impact Engineering 2010;37:317–23.
- [3] J Gibson L, Ashby MF. Cellular solids: structures and properties. Cambridge University Press; 1988.
- [4] Evans AG, Hutchinson JW, Fleck NA, Ashby MF, Wadley HNG. Prog Mater Sci 2001;46:309–27.
- [5] Kooistra GW, Deshpande VS, Wadley HNG. Acta Materialia 2004;52:4229–37.
- [6] Queheillalt DT, Wadley HNG. Acta Materialia 2005;53:303–13.
- [7] Jacobsen AJ, Carter WB, Nutt S. Advanced Materials 2007;19:3892–6.
- [8] Jacobsen AJ, Carter WB, Nutt S. Acta Mater 2007;55:6724–33.
- [9] Jacobsen AJ, Carter WB, Nutt S. Acta Mater 2007;56(2007):2540–8.
- [10] Tan PJ, Reid SR, Harrigan JJ, Zou Z, Li S. J Mech Phys Solids 2005;53:2206–30.
- [11] Jones N. Structural impact. Cambridge, UK: Cambridge University Press; 1989.
- [12] Abramowicz W, Jones N. Int J Impact Eng 1997;19:415–37.
- [13] Alexander JM. Q J Mech Appl Mathem 1960;13:10–5.
- [14] Wierzbicki T, Bhat SU, Abramowicz W. Int J Solids Struct 1992;29:3269–88.
- [15] Wierzbicki T, Abramowicz W. J Appl Mech 1983;50:727–34.
- [16] Pingle SM, Fleck NA, Deshpande VS, Wadley HNG, in preparation.
- [17] Ferri E, Antinucci E, He MY, Hutchinson JW, Zok FW, Evans AG. J Mech Mater Struct 2006;1:1345–65.
- [18] Hsu SS, Jones N. Int J Crashworthiness 2004;9:195–217.